ORIGINAL PAPER

CrossMark

Landslide detection based on height and amplitude differences using pre- and post-event airborne X-band SAR data

Jyunpei Uemoto[1] · Toshifumi Moriyama[2] · Akitsugu Nadai[1] · Shoichiro Kojima[1] · Toshihiko Umehara[1]

Abstract

The recognition of landslides and making their inventory map are considered to be urgent tasks not only for damage estimation but also for planning rescue and restoration activities. Owing to the capability of synthetic aperture radar (SAR) for day-and-night and all-weather imaging, various studies utilizing SAR data for landslide detection have been reported to date. Among the detection methods utilizing SAR data, those based on height differences accompanying landslides are attractive and should be further improved, since they can directly contribute to damage estimation through a volumetric estimation of landslides. In this context, we propose in this paper a landslide detection method utilizing height differences derived from pre- and post-event SAR digital elevation models (DEMs) combined with amplitude differences. The proposed method was applied to the landslides triggered by the 2016 Kumamoto earthquake. The application results demonstrate that SAR DEMs with a high altitudinal resolution can improve the detection ability and that the incorporation of the amplitude differences is effective for decreasing the number of false detections. Although the reliability of the proposed method is deemed moderate when evaluated on the basis of the kappa coefficients derived through an accuracy assessment, most of the outliers are correctly filtered out and large- and medium-scale landslides are detected. Therefore, the inventory maps derived from the proposed method are thought to be effective at the initial stage of planning rescue and restoration activities.

Keywords Landslide · Height difference map · Amplitude difference map · InSAR DEM

✉ Jyunpei Uemoto
juemoto@nict.go.jp

1 National Institute of Information and Communications Technology, 4-2-1, Nukui-Kitamachi, Koganei, Tokyo 184-8795, Japan

2 Graduate School of Engineering, Nagasaki University, 1-14, Bunkyo-machi, Nagasaki 852-8521, Japan

1 Introduction

According to Cruden (1991), a landslide is defined as the mass movement of rock, earth or debris down a slope. Landslides can be induced by natural events and human activities such as heavy rainfall, earthquakes, deforestation and the excavation of slopes (Dai et al. 2002). Landslides wreak havoc on human lives and infrastructures in mountainous areas (Dai et al. 2002; Metternicht et al. 2005; Scaioni et al. 2014); thus, the recognition of landslides and making their inventory map are urgent tasks not only to support damage estimation but also to plan rescue and restoration activities (Plank 2014; Plank et al. 2016). Owing to its capability of wide-area observation, remote sensing based on spaceborne and airborne sensors is a powerful tool for performing this task. Landslide recognition has been performed using various remotely sensed data such as optical passive sensor data, thermal infrared data, laser scanning data and synthetic aperture radar (SAR) data (Scaioni et al. 2014).

SAR data hold a unique position among these remotely sensed data owing to the capability of SAR for day-and-night and all-weather imaging. The processed SAR data are expressed as a complex image that consists of amplitude and phase at each resolution pixel (Oliver and Shaun 2004). The amplitude data alone can be directory utilized for visual interpretation. On the other hand, the phase data are often combined with two or more SAR data acquired from similar orbits to derive a digital elevation model (DEM) through the interferometric SAR (InSAR) technique, as well as to derive minute changes in the slant range direction through the differential InSAR (DInSAR) technique (Lu et al. 2010). Moreover, polarimetric SAR data have been studied for terrain and land use classification. Various studies utilizing SAR data for landslide detection and characterization have been reported, even for these ten years (e.g., Cao et al. 2008; Liao and Shen 2009; Christophe et al. 2010; Dong et al. 2011; Kawamura et al. 2011; Furuta and Sawada 2013; Zhao et al. 2013; Liu and Yamazaki 2015; Shibayama et al. 2015; Tang et al. 2015; Plank et al. 2016).

These methods can be roughly classified into two groups: those dependent on the coherency of coevent SAR data and those that are not. One of the advantages of the former is that they can treat surface changes or movements smaller than the wavelength of a SAR system. For example, Zhao et al. (2013) analyzed the L-band Advanced Observing Satellite (ALOS) Phased Array-type L-band SAR (PALSAR) using the short baseline subset (SBAS) InSAR. They detected pre-rockslide movement of less than 50 cm within 184 days for the 2009 Jiweshan rockslide in China. However, the requirement of coherency between coevent data imposes a severe constraint on their spatial and temporal baselines. On the other hand, for the latter methods, the constraint on the baselines is less rigorous, although the scale of the phenomena that they can treat depends on the spatial resolution of the SAR system, which generally becomes coarser than those of the coherency-based methods. For example, to detect landslides in combination with a slope map derived from an external DEM, Liu and Yamazaki (2015) analyzed and visually assessed the difference in polarimetric backscattering coefficients for the coevent data obtained from different airborne L-band SAR sensors having a time lag of more than 10 years. Their research indicated that the coherency-independent methods have more chances of being applied to landslides detection than the coherency-dependent ones. Moreover, Plank et al. (2016) proposed and assessed quantitatively a landslide detection method that utilized high-resolution satellite optical imagery as the pre-event data and very high-resolution satellite SAR imagery as the post-event data.

Now, we further classify the coherency-independent methods into two groups on the basis of their viewpoints: One viewpoint is the land cover change, and the other is the height change in association with landslides. The former methods assume that landslides replace vegetated areas with bare soil or rock. However, such a land cover change can be triggered not only by landslides but also by human activities such as the cultivation of flatlands. Thus, some previous studies involved attempts to filter out the detected land cover changes independent from landslides using a slope map calculated from an external DEM or a post-event SAR DEM (e.g., Cao et al. 2008; Liu and Yamazaki 2015; Plank et al. 2016). On the other hand, the latter methods treat the height changes of landslides. Arturi et al. (2003) generated a post-event SAR DEM from the European Remote Sensing (ERS)-1 and ERS-2 tandem pairs and subtracted it from an external pre-event DEM. They mentioned that the DEM differences showed a good fit to landslide features qualitatively, although they also showed strong differences where the landslide did not produce evaluable effects. The methods utilizing the SAR DEM seem to be attractive since they may successively contribute to damage estimation through a volumetric estimation of landslides and thus to the planning of subsequent rescue and restoration activities. To improve the detection accuracy of landslides from the subtraction of pre- and post-event DEMs, the following two ideas can be pointed out. The first is to incorporate other factors given that the landslide detection methods based on land cover changes are often combined with a slope map. This would contribute to a decrease in the number of false detections. The second is to utilize more accurate DEM datasets. For example, to generate a height change map for the 2009 Jiweshan rockslide, Zhao et al. (2013) generated a SAR DEM by stacking several post-event ALOS InSAR data and then subtracted Shuttle Radar Topography Mission (SRTM) DEM from the obtained SAR DEM. They reported that the accuracy of their height change map is approximately 14 m. Tang et al. (2015) also generated a height change map and performed a volumetric estimation for the 2008 Wenjiagou landslide using SRTM and SAR DEM calculated from TerraSAR-X and TanDEM-X.

Considering the aforementioned two ideas, in this paper, we propose a landslide detection method utilizing height differences derived from pre- and post-event SAR DEM combined with amplitude differences. The rest of this paper is organized as follows. In Sect. 2, we introduce a study event and datasets. The proposed method is described in Sect. 3. In Sect. 4, we demonstrate the proposed method and discuss the application results. Finally, conclusions are given in Sect. 5.

2 Study area and datasets

A large earthquake, called the 2016 Kumamoto earthquake, occurred on April 16, 2016, at 01:25 JST (Japanese standard time, JST = UTC + 9 h) in Kyusyu, Japan. The epicenter and magnitude of this earthquake were 32.8°N, 130.8°E and M7.3, respectively, as determined by the Japan Meteorological Agency (Yagi et al. 2016). Yagi et al. (2016) constructed a rupture process model of this earthquake. According to their model, the mainshock rupture mainly propagated northeastward from the epicenter and terminated near the southwest side of Aso volcano. A large number of landslides occurred because of this earthquake. In addition to field surveys, various observations such as aerial and satellite photographs and SAR data acquisition and aerial laser scanning were performed after this earthquake occurred.

The National Institute of Information and Communications Technology (NICT) performed SAR observation on April 17, 2016, the day after the earthquake occurred, using the airborne X-band SAR called Pi-SAR2, which has been developed by NICT since 2006 (Nadai et al. 2009). Pi-SAR2 is a left-side-looking SAR having the capabilities of full polarimetric and cross- and/or along-track interferometric observations (XTI and/or ATI) simultaneously (Kojima et al. 2014). Among the operation modes of Pi-SAR2, the finest spatial resolution of 0.3 m is achieved when operated in modes 0 and 1. In these operation modes, the center frequency and bandwidth are 9.55 GHz and 500 MHz, respectively. Pi-SAR2 collects XTI data using the main and subantennas suspended separately at the base of the left and right wings of a Gulfstream II aircraft. The baseline length for XTI is approximately 2.6 m, and the standard deviation of height measurement of XTI was estimated as 2.4 m using corner reflectors on a runway in a preliminary evaluation (Kobayashi et al. 2012).

NICT performed coincidentally a Pi-SAR2 observation at Aso volcano and its surroundings on December 5, 2015, approximately 4 months before the earthquake. The purpose of this observation at that time was to monitor the activity of Aso volcano. In response to the existence of this pre-earthquake observation, some of the platform orbits on April 17, 2016, were set to follow the pre-earthquake observation that resulted in the acquisition of pre- and post-event SAR data pairs for the earthquake. The observation parameters of pre- and post-event data pairs analyzed in this paper are listed in Table 1. The area of each scene is 2 km in the ground range and 1 km in the azimuth direction. Owing to the perturbation of platform orbits, some parameters such as platform altitude and baseline between pre- and post-event data differ for each scene, even though these scenes were cut from the same stripmaps. Thus, the parameters are listed for each scene in Table 1.

Figure 1 shows the aerial photographs corresponding to the scenes listed in Table 1. These photographs were taken by the Geospatial Information Authority of Japan (GSI) on April 16, 2016, one day before the Pi-SAR2 observation. In this paper, as the truth data, we adopted the polygon data for landslides based on the visual interpretation of photograph data released by the National Research Institute for Earth Science and

Table 1 Observation parameters for pre- and post-event data

Parameters	Scene A		Scene B		Scene C	
	Pre-event	Post-event	Pre-event	Post-event	Pre-event	Post-event
Observation ID	2015120515	2016041709	2015120515	2016041709	2015120515	2016041709
Platform altitude	8945.9 m	8993.5 m	8948.0 m	8992.5 m	8946.3 m	8989.3 m
Platform azimuth angle	-89.9 °	-89.9 °	-90.0 °	-90.0 °	-90.0 °	-90.0 °
Incident angle at nearest range	50.8 °	50.2 °	37.9 °	37.1 °	36.1 °	35.2 °
Incident angle at farthest range	55.4 °	54.9 °	45.1 °	44.4 °	43.6 °	42.8 °
Baseline between pre- and post-event	191.6 m		186.9 m		183.7 m	
Pixel number in slant range direction	8550	8485	7093	6981	6856	6739
Pixel number in azimuth direction	4000					
Pixel spacing	0.19 m in slant range × 0.25 m in azimuth directions					

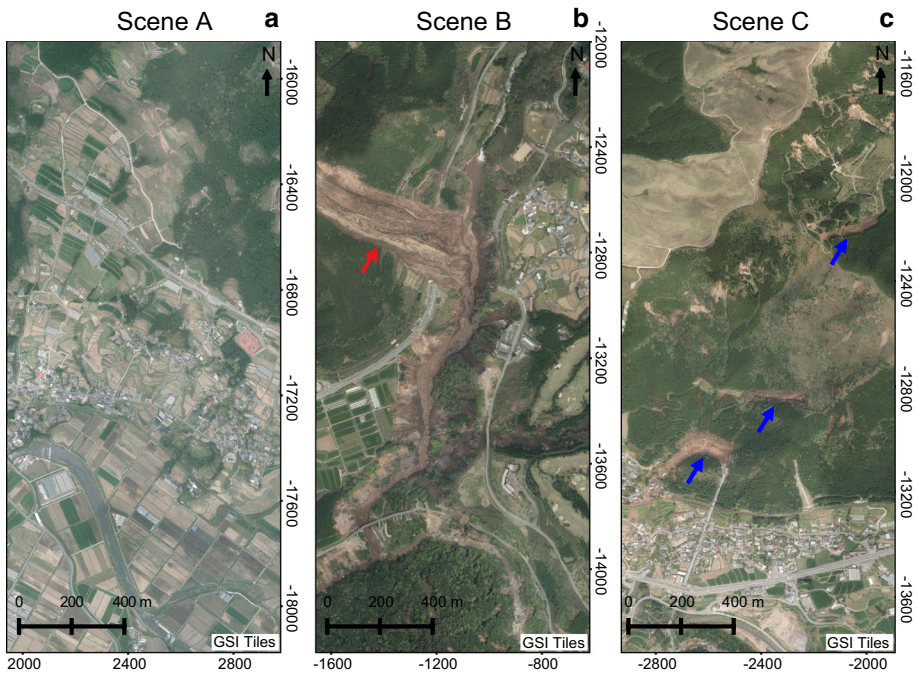Note that the platform altitude is geoid-height corrected values

Fig. 1 Aerial photographs taken by GSI on April 16, 2016, one day before Pi-SAR2 observation. The red and blue arrows are added to indicate the landslides regarded as large- and medium-scale ones in this paper: **a** Scene A; **b** Scene B; **c** Scene C

Disaster Resilience (NIED.) The landslide features in each scene are briefly summarized as follows: In Scene A (Fig. 1a), no landslides are identified in the truth data. In Scene B (Fig. 1b), a large-scale landslide, indicated by the red arrow, occurred in the upper left region, and slope failures occurred along the gullies from north to south and from west to east in the center region. In Scene C (Fig. 1c), three medium-scale landslides, indicated by the blue arrows, occurred in the middle region and some small-scale landslides occurred mainly in the upper left region. The proposed method described in the next section is applied to these scenes.

3 Methods

The schematic images of the proposed method are shown in Fig. 2. The datasets required for this method are single-look slant range complex (SSC) pairs for XTI processing in pre- and post-events. Each pair consists of master and slave data collected in the vertical polarization and referred to as VV_m and VV_s, respectively. The pulses were transmitted from the main antenna for both the master and slave data. On the other hand, the backscattered signals were received at the main antenna for the master data and at the subantenna for the slave data. Namely, the SSC pairs utilized in the proposed method are the dataset for bistatic XTI. The proposed methods can be divided into four parts: the data processing
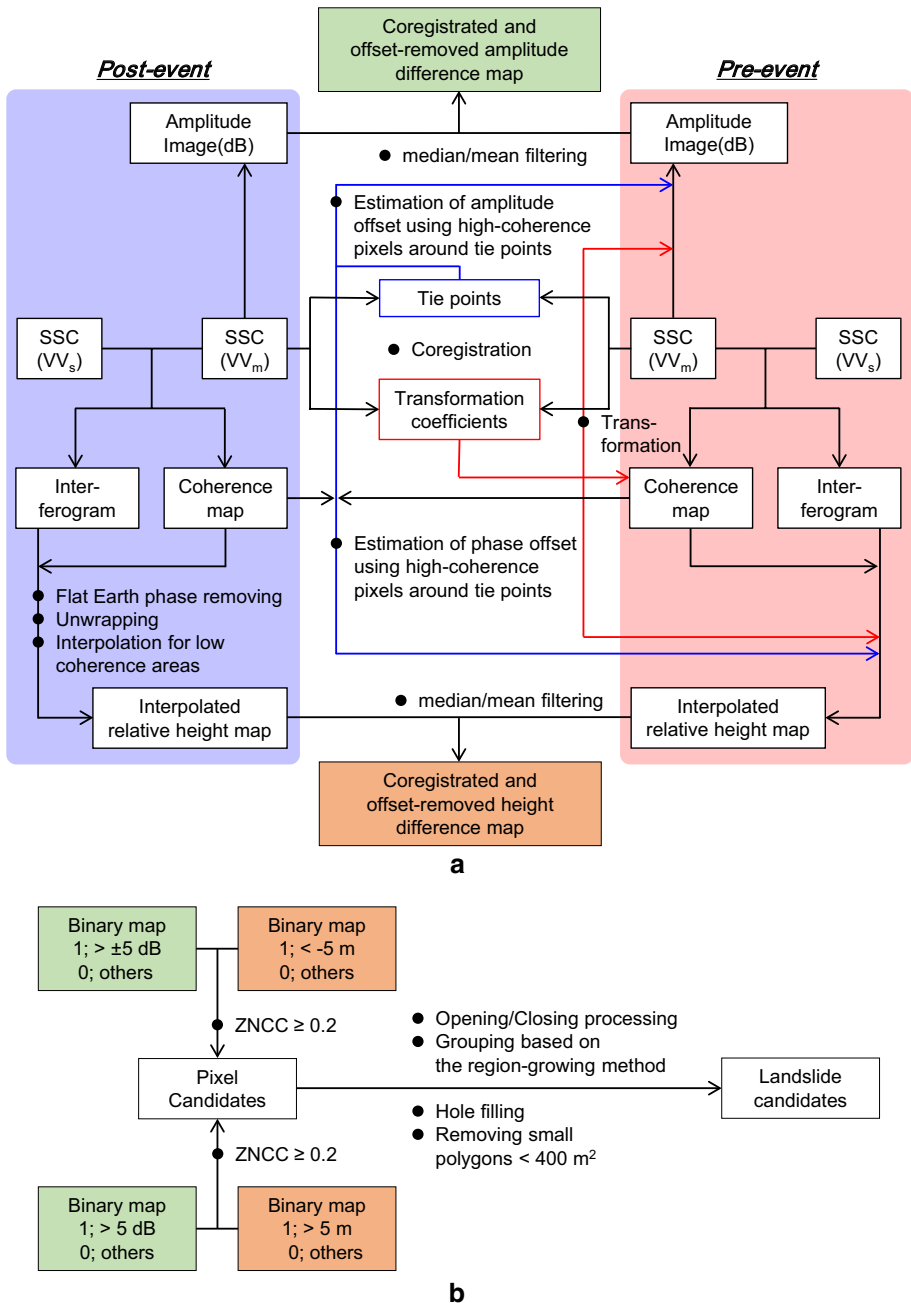
Fig. 2 Schematic images of the proposed method: **a** processing for generation of amplitude and height difference maps, **b** fusion processing for landslide detection

for each pre- and post-event data, the coregistration processing between pre- and post-event data, difference processing and fusion processing. In the rest of this section, we first

introduce the expected features of landslides in the height and amplitude differences and then describe each processing part. Note that the window sizes for coherence, median and mean filtering are set to be 9×9 pixels that corresponds to 1.71 m in slant range $\times 2.25$ m in azimuth directions. Including these window sizes, the value of parameters and thresholds required for the proposed method was empirically chosen to give satisfactory pre-experiment results.

3.1 Landslide features on amplitude and height difference maps

The expected features of landslides on the height and amplitude difference maps are as follows: At the source area, the ground is gouged, and thereby, the height decreases. At the same time, land cover objects such as trees are scoured away. This results in the increase in the amplitude of vertical polarization since the land cover change from vegetation to bare soil or rock makes the surface scattering dominant. In addition, steep slopes might form, resulting in the formation of radar shadow areas where tree canopies were observed in the pre-event data. Therefore, the amplitude can increase or decrease. On the other hand, at the deposit area, flowed-in soil or rock is heaped on the former land cover objects. Then, the height increases and the amplitude also increases. On the basis of the consideration mentioned above, the landslide features are summarized into the following three patterns: The height decreases and the amplitude increases, the height decreases and the amplitude also decreases, and the height increases and the amplitude also increases. The proposed method is designed to extract these three patterns. Note that meaningful information cannot be extracted from low-coherence areas in both pre- and post-event data. Thus, we define the coherence threshold of 0.8 to exclude these areas from landslide detection.

3.2 Data processing for each pre- and post-event data

First, pre- and post-event raw data are processed into the SSC data pairs aligned in the same azimuth direction as performed by Kobayashi et al. (2016). This alignment reduces the rotational component of the affine conversion so that we can effectively narrow down the extent of the search area for tie points. Next, the interferogram and VV_m amplitude image in the logarithmic scale are processed for each pre- and post-event. The coherence map, a by-product of InSAR processing, is utilized for quality validation in the latter processes. After the interferogram generation, flat-earth phase removal and phase unwrapping are performed. In this study, the minimum L^p-norm algorithm (Ghiglia and Pritt 1998) is adopted for the phase unwrapping. The height values are converted from the unwrapped phase differences (Richards 2007):

$$h(p) = h_0 + \alpha_{IF}(p)\big(\phi(p) - \phi_0\big), \tag{1}$$

where $h(p)$ and $\phi(p)$ are the true height and phase difference at point p, respectively. The constants h_0 and ϕ_0 are used to convert the relative height into the true one; as expressed in Eq. (1), when $\phi(p)$ is equal to ϕ_0, $h(p)$ becomes h_0. The coefficient of $\alpha_{IF}(p)$ is the interferometric scale factor (Richards 2007) expressed as

$$\alpha_{IF}(p) = \frac{\lambda H \, \cot \psi(p)}{n\pi B \, \sin \psi(p)}, \tag{2}$$

where λ, H, B and $\psi(p)$ are the wavelength of a SAR system, the platform altitude, the baseline length and the depression angle at point p, respectively. Note that the baseline is assumed to be horizontally located in Eq. (2). The constant n in the denominator depends on the form of XTI observation. As mentioned above, the SSC pairs utilized in the proposed method are for bistatic XTI so that n is equal to 2. The phase difference values of the interferogram are doubtful in the low-coherence areas (Massonnet and Feigl 1998) such as the radar shadows, roads and water surfaces. Thus, we perform linear interpolation for the height values in such areas along the slant range direction.

3.3 Coregistration between pre- and post-event data

A coregistration process is required to derive any differences between pre- and post-event data. The coregistration processing in the proposed method is based on the algorithm reported by Tobita et al. (1999). Their algorithm estimates the affine coefficients between amplitude images based on the magnitude of cross-correlation (CC) around the automatically selected tie points. One of the advantages of their method is the refinement of the matching accuracy through the iterative elimination of erroneous tie points. Generally, the variation of incident angle within the swath width is not negligible for airborne SARs. Thus, in addition to the normal affine conversion, our coregistration process takes the distortion caused by this incident angle variation into consideration. For the latter processes, we exclude tie points having a low magnitude of the zero-mean normalized CC (ZNCC) coefficient. The ZNCC coefficient of $z(x, y)$ at the position of $p(x, y)$ between the amplitude image of $A_m(x, y)$ and the another one of $A_s(x, y)$ shifted by (x', y') is expressed as

$$z(x, y) = \frac{\sum_{i=x-M}^{x+M} \sum_{j=y-N}^{y+N} \left\{ A_m(i,j) - \overline{A_m} \right\} \left\{ A_s(i+x', j+y') - \overline{A_s} \right\}}{\sqrt{\sum_{i=x-M}^{x+M} \sum_{j=y-N}^{y+N} \left\{ A_m(i,j) - \overline{A_m} \right\}^2} \sqrt{\sum_{i=x-M}^{x+M} \sum_{j=y-N}^{y+N} \left\{ A_s(i+x', j+y') - \overline{A_s} \right\}^2}},$$
(3)

where M and N define pixel numbers of window and A_m and A_s are amplitude values, respectively. $\overline{A_m}$ and $\overline{A_s}$ are averaged amplitude values defined as

$$\overline{A_m} = \frac{1}{(2M+1)(2N+1)} \sum_{i=x-M}^{x+M} \sum_{j=y-N}^{y+N} A_m(i,j)$$
(4a)

and

$$\overline{A_s} = \frac{1}{(2M+1)(2N+1)} \sum_{i=x-M}^{x+M} \sum_{j=y-N}^{y+N} A_s(i+x', j+y').$$
(4b)

As performed in Tobita et al. (1999), the coefficient is refined through FFT over-sampling. After estimating the transformation coefficients between the pre- and post-event amplitude images, we transform the pre-event products. The bicubic interpolation method is used in this transformation. Note that the areas are excluded for landslide detection in the latter processes where the bicubic interpolation cannot be applied, for example, neighborhoods to the edges of an image.

3.4 Difference processing

In this step, we estimate the offsets in the relative height maps between the pre- and post-events as well as in the amplitude images at first. Figure 3 shows the amplitude images of
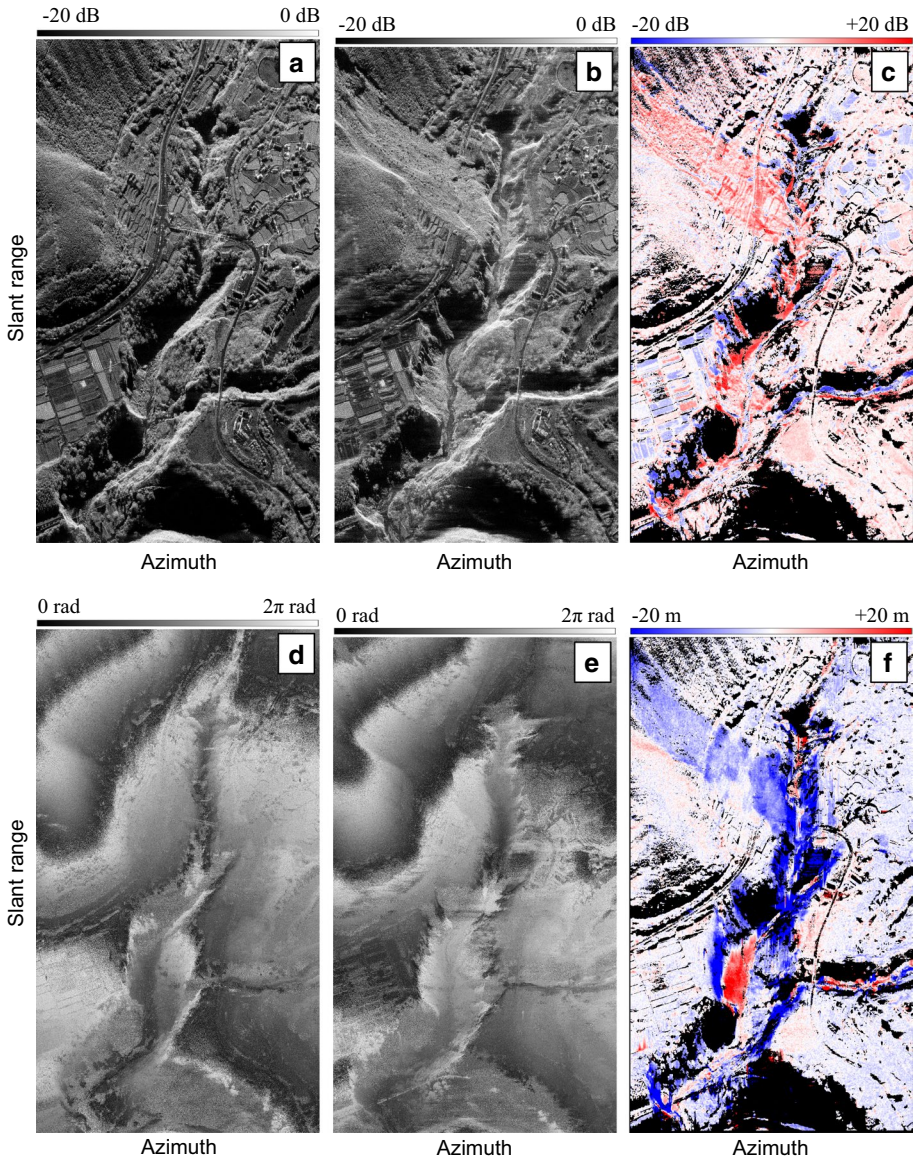

Fig. 3 Amplitude images of VV_m, flat-earth phase removed interferograms and difference maps in the pre- and post-events for Scene B. In the difference maps, values are derived from subtracting the pre-event values from the post-event ones and black-colored areas indicate those excluded from landslide detection. **a** Amplitude image in the pre-event, **b** amplitude image in the post-event, **c** amplitude difference map, **d** interferogram in the post-event, **e** interferogram in the pre-event, **f** height difference map

VV_m, flat-earth phase removed interferograms and difference maps in the pre- and post-events for Scene B as reference. On the basis of Eq. (1), the height maps in the pre- and post-events are expressed as

$$h_{\text{pre}}(p) - h_{0,\text{pre}} = \alpha_{\text{IF,pre}}(p)\big(\phi_{\text{pre}}(p) - \phi_{0,\text{pre}}\big) \tag{5a}$$

and

$$h_{\text{post}}(p) - h_{0,\text{post}} = \alpha_{\text{IF,post}}(p)\big(\phi_{\text{post}}(p) - \phi_{0,\text{post}}\big), \tag{5b}$$

where the subscripts pre and post denote the pre-event and post-event, respectively. Let $h_{\text{pre}}(p)$ be 0 when $\phi_{\text{pre}}(p)$ is equal to 0, and then, Eq. (5a) is modified to

$$h_{\text{pre}}(p) = \alpha_{\text{IF,pre}}(p)\phi_{\text{pre}}(p). \tag{5c}$$

This approximation yields an additional gradient along the slant range and prevents us from deriving the true height map in the pre-event. However, this is a good approximation because what we need to estimate is not the absolute height maps in both the pre- and post-events, but the relative height changes between them. The height difference at point p can be derived by subtracting Eqs. (5c) from (5b):

$$h_{\text{dif}}(p) = \alpha_{\text{IF,post}}(p)\big(\phi_{\text{post}}(p) - \phi_{0,\text{post}}\big) - \alpha_{\text{IF,pre}}(p)\phi_{\text{pre}}(p), h_{\text{dif}}(p) \equiv \big(h_{\text{post}}(p) - h_{0,\text{post}}\big) - h_{\text{pre}}(p), \tag{6}$$

On the basis of Eq. (6), when $h_{\text{dif}}(p)$ is equal to 0, we can estimate $\phi_{0,\text{post}}$ as

$$\phi_{0,\text{post}} = \phi_{\text{post}}(p) - \frac{\alpha_{\text{IF,pre}}(p)}{\alpha_{\text{IF,post}}(p)}\phi_{\text{pre}}(p). \tag{7}$$

As expressed in Eq. (6), it is necessary to determine $\phi_{0,\text{post}}$ to estimate $h_{\text{dif}}(p)$. Now, the problem is to seek the areas where the condition that $h_{\text{dif}}(p)$ is equal to 0 are satisfied. When taking the possibility of speckle noise contamination into consideration, it is inexpedient to calculate Eq. (7) at a certain point. However, the estimation of $\phi_{0,\text{post}}$ from the whole area still seems insufficient. The reason is that $h_{\text{dif}}(p)$ is not equal to 0 in the areas where landslides occurred and the vegetation changed seasonally. In this context, we utilize the values at pixels showing a high coherence around the resultant tie points. As mentioned in Sect. 3.3, we exclude tie point candidates having a low ZNCC coefficient. This is because we can expect a high ZNCC coefficient at the areas where no changes occurred between the pre- and post-events. On the basis of this expectation, we estimate $\phi_{0,\text{post}}$ by averaging the right side of Eq. (7) around the tie points mentioned above. In addition to the phase offset, the amplitude offset is estimated in the same manner. Finally, through median and mean filtering, we acquire the coregistrated and offset-removed difference maps of height and amplitude. Note that the areas are excluded for landslide detection where the relative height is not obtained in the pre- or post-event.

3.5 Fusion processing

Figure 4 shows the histograms of the amplitude (Fig. 4a) and height differences (Fig. 4b) for Scene A where no landslides have been identified in the truth data. These differences
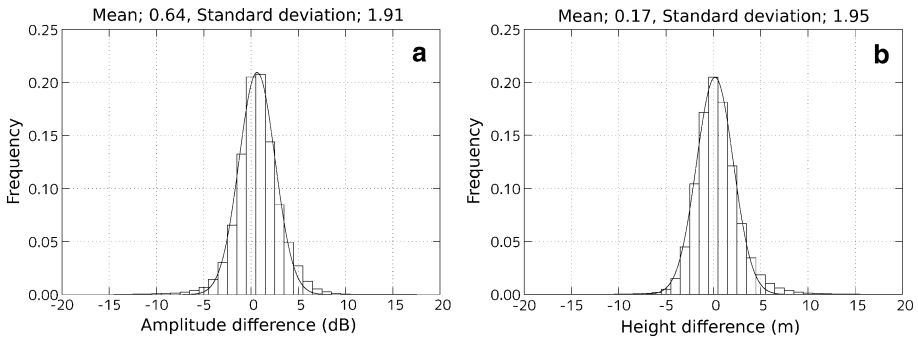
Fig. 4 Histograms of difference at Scene A. Mean and standard deviation values resulted from fitting the normal distribution curve are indicated at the top of each panel: **a** amplitude difference, **b** height difference

are derived from subtracting the pre-event values from the post-event ones. The curve in each panel corresponds to the fitted normal distribution function. As shown in Fig. 4a, b, each histogram is well fitted with the normal distribution function. The mean and standard deviation for the amplitude difference map are approximately 0.6 dB and 1.9 dB, while those for the height difference map are 0.2 m and 2.0 m, respectively. These indicate that the offset estimation method described in Sect. 3.4 works well. The width and offset from the center of each histogram indicate the limitation of differences that we can detect using the proposed method and/or the Pi-SAR2 system. On the basis of the mean and standard deviation values, we utilize only the pixels having absolute values greater than the thresholds. The threshold for amplitude is 5 dB and that for height is 5 m.

To fuse the height and amplitude differences, we calculate the ZNCC coefficient between them in the proposed method. Thresholding based on the ZNCC coefficient is expected to be effective for noise reduction, since there is no need for the unchanged areas to correlate with each other. To do so, the height and amplitude difference maps are binarized using the thresholds mentioned above; then, the ZNCC coefficients are calculated for the three patterns described in Sect. 3.1. The pixels having a ZNCC coefficient of 0.2 and more are regarded as the candidate areas of landslides. The candidates are then segmented into polygons based on the region-growing method after performing opening and closing processes. Finally, as performed by Liu and Yamazaki (2015) and Plank et al. (2016), small blocks less than 400 m^2 are excluded.

4 Results and discussion

In this section, we describe and discuss the results of the application of the proposed method to the scenes listed in Table 1.

4.1 Amplitude differences

Figure 5 shows the amplitude difference maps for Scenes A, B and C. Red and blue indicate the points at which the amplitude increased and decreased, respectively. The areas

excluded from the landslide detection are colored white. The landslides in Fig. 1 can be recognized in Fig. 5 as aggregations of the red or blue points. Even the small-scale landslides can be recognized, for example, in the upper left region of Fig. 5c. The large-scale landslide in the upper left region of Fig. 1b is clearly colored red in Fig. 5b. This is due to the surface changes from the vegetated land cover into the bare soil or rock, and this is consistent with the assumption of landslide detection methods based on the polarization changes (e.g., Cao et al. 2008; Plank et al. 2016). It is worth noting that some landslides are indicated by the red and blue areas close to each other, for example, the landslides at the center and left lower parts of Fig. 5c. From the comparison between the aerial photograph in Fig. 1c with Fig. 5c, it can be seen that the blue areas are located at a higher altitude than the red ones. This results from the steep slope formation accompanying the land cover objects such as trees being scoured away. The blue regions correspond to the radar shadows. In addition to the areas where the landslides occurred, red and blue points are also seen at the areas where no landslides are identified, remarkably in the lower part of Fig. 5a, b. By a visual interpretation of Fig. 1a, b, we can identify these areas as fields for cultivation or residential areas. As listed in Table 1, the pre-event data were acquired in December, whereas the post-event data were acquired in April. Thus, some parts of them result from a difference in the growth stage of cultivated crops. On the other hand, the gullet in Fig. 5b becomes wider owing to the slope failures accompanying the earthquake. This suggests that the flat areas in the pre-event have changed into slopes or walls. Thus, it can be understood that the filtering out of outliers based on slope angles derived from a pre-event DEM does not always work well. This fact is consistent with the claim of Lu et al. (2010)
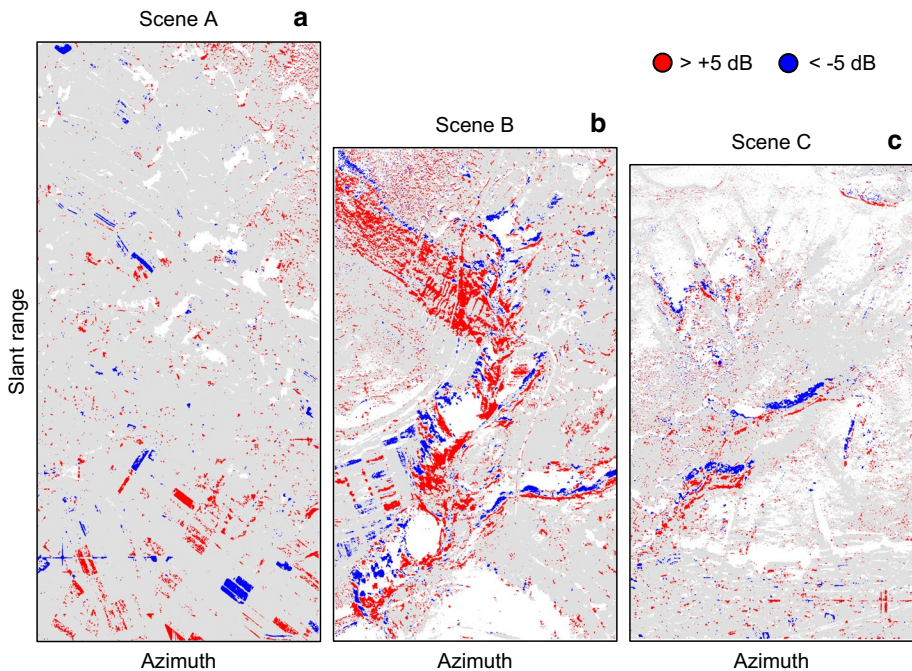

Fig. 5 Amplitude difference maps. Areas for analysis are colored gray. The color code of amplitude differences is shown in the legend at the upper right: **a** Scene A, **b** Scene B, **c** Scene C

that a timely DEM can be critical for hazard assessments. At the same time, this fact also indicates the importance of post-event DEM acquisition. The datasets described in Sect. 2 include both the pre- and post-event DEMs obtained from the bistatic XTI so that such a slope failure can be detected in this study.

4.2 Height differences

Figure 6 shows the height difference maps for Scenes A, B and C. As is the case in Fig. 5, red and blue indicate the points at which the height increased and decreased, respectively. In Fig. 6, the areas above and below the height thresholds of ± 20 m are highlighted in yellow and light blue, respectively. The threshold of 20 m corresponds to the lower limit for landslide detection adopted by Arturi et al. (2003). As seen in Fig. 6, the landslides analyzed in this paper become difficult to identify except for a few cases, if we adopt the threshold of 20 m. This fact supports our idea described in Sect. 1 that accurate DEM datasets improve the accuracy of a DEM-based landslide detection. However, the small-scale landslides seen in Fig. 5 cannot be seen in Fig. 6. This fact implies that the height changes accompanying small-scale landslides are below the threshold of 5 m and that this threshold may still be insufficient. We discuss this matter in the last part of this section.

Except for small-scale landslides, the areas of the landslides as well as the slope failures are colored in Fig. 6. Most areas are colored blue. The red-colored area that stands out is at the middle part in Fig. 6b at the most. From a comparison between Figs. 6b and
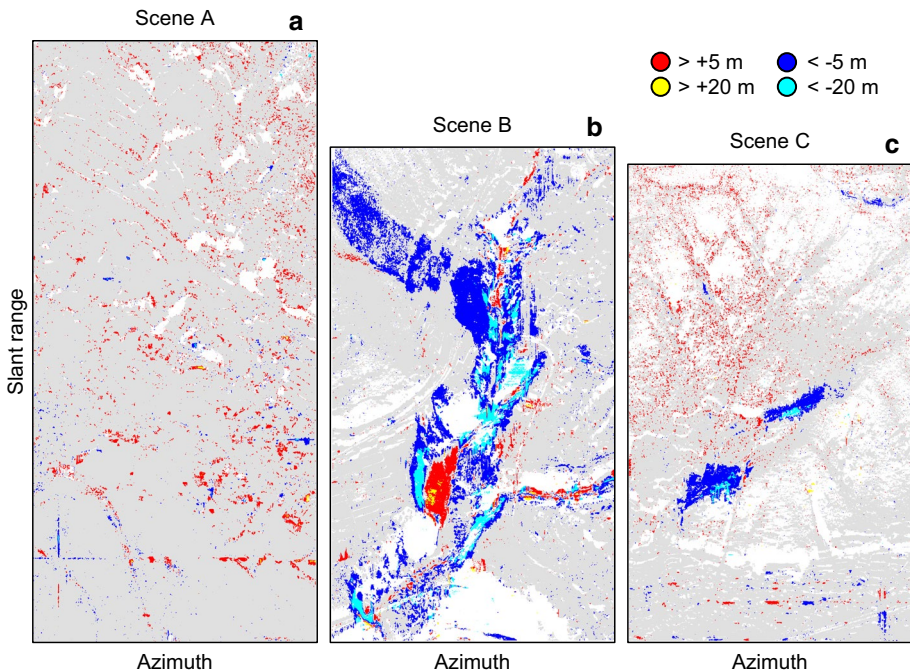

Fig. 6 Height difference maps. Areas for analysis are colored gray. The color code of height differences is shown in the legend at the upper right: **a** Scene A, **b** Scene B, **c** Scene C

1b, this red-colored area can be recognized as a piled up area of flowed-in soil. However, we can find no such area around the gullet. This might be due to the existence of radar shadows. The cultivation areas, which are prominent in Fig. 5a, b, are scarcely colored in Fig. 6a, b. In addition, although the residential areas are colored in spots, the coherence between the amplitude and the height difference maps appears to be not so high.

4.3 Fused differences

A common feature that can be seen in Figs. 5 and 6 is that the colored pixels are scattered throughout the entire scenes. One of the reasons is the existence of outliers that cannot be removed by the median and mean filtering. In addition, for the height difference maps, the baseline errors, such as the length and angle, are considerable because we estimate the phase offset between the pre- and post-event interferograms, but the baseline errors are not estimated in the proposed method. To eliminate the remaining outliers, we fuse the height and amplitude difference maps with the procedure described in Sect. 3.5. Figure 7 shows the fused maps for Scenes A, B and C. Black dots are candidates of landslides having a ZNCC coefficient above the threshold. Most of the cultivation and residential areas are filtered out by performing the ZNCC calculation. In addition, the number of mottled outliers is reduced considerably. These facts support our idea described in Sect. 1 that the incorporation of other factors into a DEM-based landslide
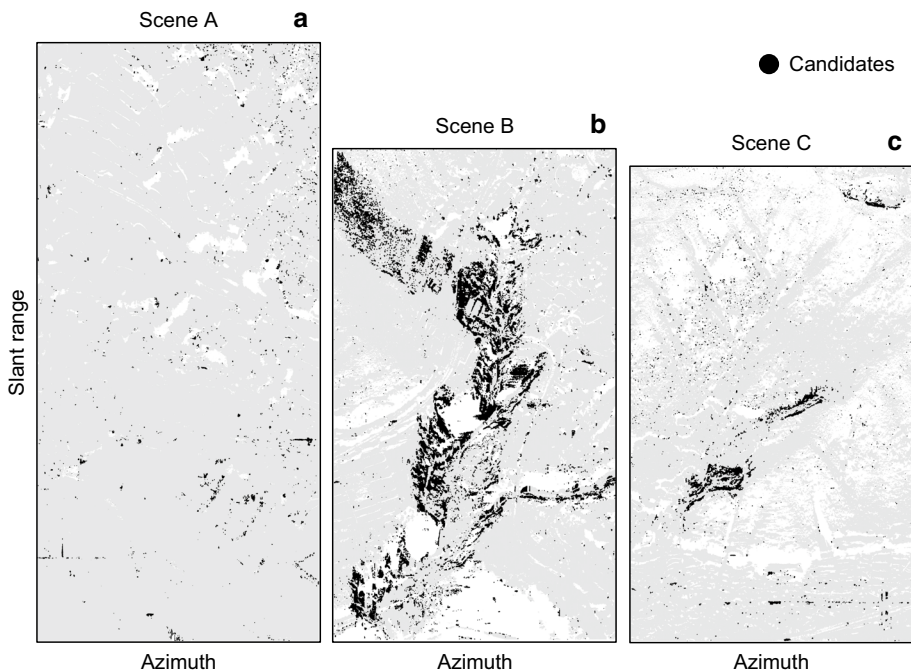

Fig. 7 Candidates of landslides derived through calculation of ZNCC between amplitude and height difference maps shown in Figs. 4 and 5. Candidates are colored black. Areas for analysis are colored gray: **a** Scene A, **b** Scene B, **c** Scene C

detection improves the detection accuracy. Figure 8 shows the final product of the proposed method for Scenes A, B and C. To obtain these products, the candidates in Fig. 7 are segmented into polygons after the opening and closing processes and the area-based noise reduction, as described in Sect. 3.5.

4.4 Accuracy assessment

To perform an accuracy assessment, we compare the detected landslides shown in Fig. 8 with the polygon data of landslides released by NIED. The NIED polygon data are based on visual photograph data interpretation. For comparison, we orthorectify the detected landslides shown in Fig. 8 using the external DEM of Fundamental Geospatial Data provided by GSI and then polygonize them. Note that treating very small polygons is difficult in the accuracy assessment; thus, we also apply the same opening and closing processes to the excluded areas shown as white, which are equivalent to the gray areas in Figs. 5, 6, 7 and 8. Figure 9 shows the comparison between the detected landslide polygons and the truth ones. The areas of true positive, false positive, false negative and true negative are shown in different colors, as indicated by the legend at the bottom. Table 2 shows the confusion matrices with the overall accuracies, producer's and user's ones and the kappa coefficients. The confusion matrix for Scene A is not shown because no landslides are identified in the truth data. The user's accuracy corresponds
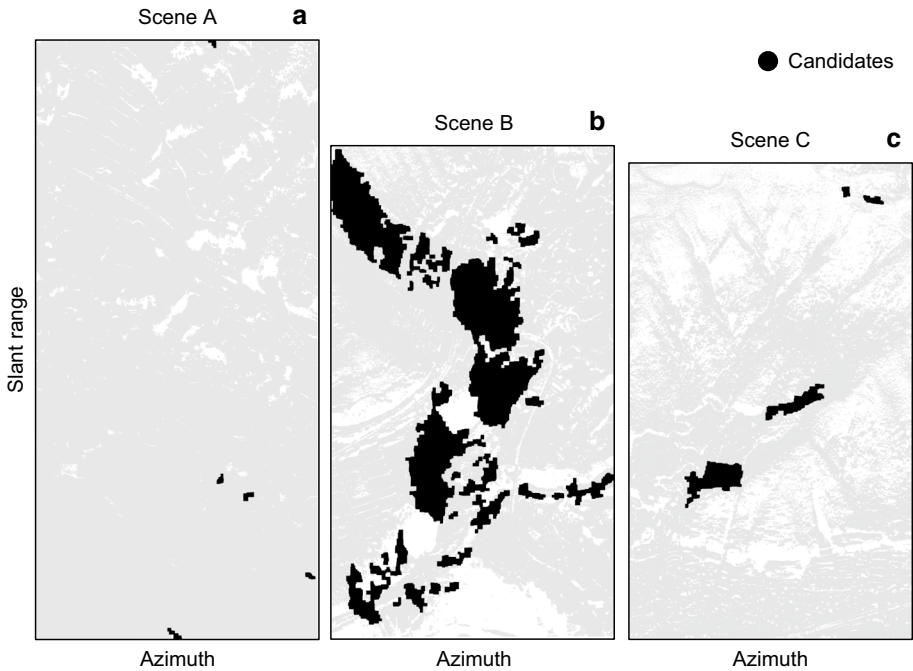

Fig. 8 Results of landslide detection. Detected landslides are colored black. Areas for analysis are colored gray: **a** Scene A, **b** Scene B, **c** Scene C
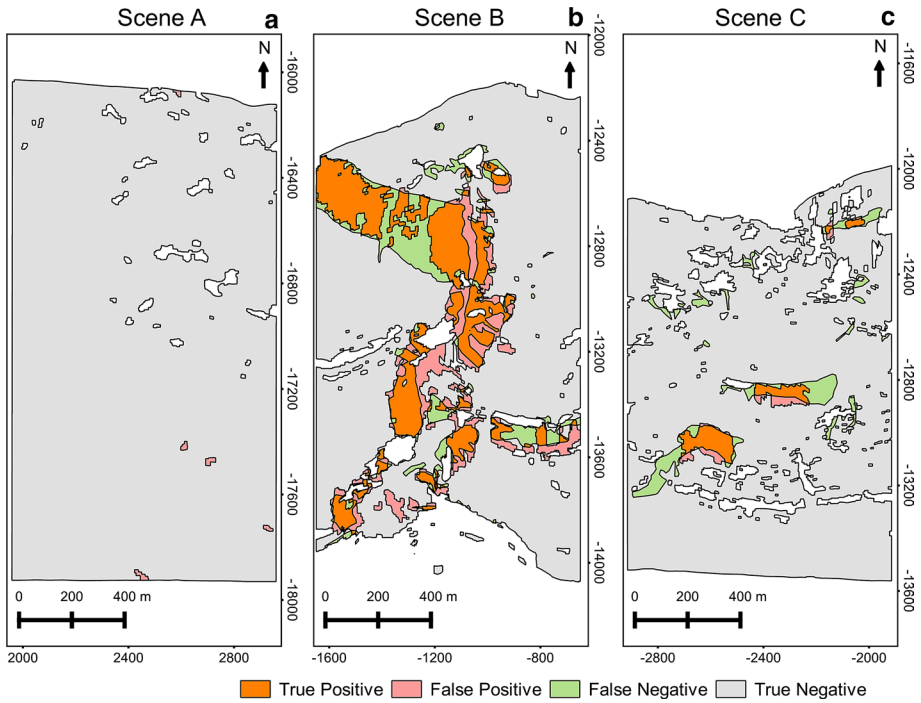
Fig. 9 Comparison between the truth data and detection maps of landslide. The color code is shown in the legend at the bottom: **a** Scene A, **b** Scene B, **c** Scene C

Table 2 Confusion matrices with the overall, producer's and user's accuracies and the kappa coefficient for Scenes B and C

Scene B		Detected (ha)		Total	Producer's accuracy (%)
		Landslides	Others		
Actual (ha)	Landslides	20.4	9.1	29.5	69
	Others	10.1	112.5	122.6	92
Total		30.5	121.6	152.1	
User's accuracy (%)		67	93		
Overall accuracy (%)		87	Kappa coefficient		0.60

Scene C		Detected (ha)		Total	Producer's accuracy (%)
		Landslides	Others		
Actual (ha)	Landslides	2.7	4.7	7.4	36
	Others	1.0	118.2	119.2	99
Total		3.7	122.9	126.6	
User's accuracy (%)		72	96		
Overall accuracy (%)		95	Kappa coefficient		0.46

to the ratio of correctly detected landslides to all the detected ones, while the producer's accuracy corresponds to the ratio of detected landslides to the actual ones. The kappa coefficient is an index for comparing the observed reliability with the one obtained by chance. The closer the kappa coefficient is to 1, the more reliable the observed accuracy. Congalton (1991), for example, reviewed in detail the accuracy assessment using the confusion matrix.

The overall accuracies and kappa coefficients for Scenes B and C are 87%, 0.60 and 95%, 0.46, respectively. On the basis of these kappa coefficients, the reliability of the proposed method is evaluated as moderate. It is worth noting that the producer's accuracy in Scene C is noticeably low. This is because of two reasons: One is that the small-scale landslides are not detected, and the other is the imperfect detection of the medium-scale landslides. The detected areas for medium-scale landslides are half of them at best, as seen in Fig. 9c. As shown in Fig. 6c, it can be seen that these landslides are not properly identified in the height difference map. This means that the height difference of a part of medium-scale landslides is measured as not greater than the threshold of 5 m in addition to the small-scale ones. The following two possibilities can be considered. One is that the height difference is actually not greater than the threshold. The height can decrease when the land cover objects such as trees are scoured away, while it can increase when flowed-in soil or rock accumulates. Their synergistic effects result in the decrease in the magnitude of height changes. The other reason is possibly the limitation of height measurement accuracy. The baseline errors are not estimated, the offset phase of $\phi_{0,\mathrm{pre}}$ in Eq. (5a) is enforced to be 0, and we only estimate the offsets independent from the pixel positions in the proposed method, as mentioned in Sect. 3.4. Thus, the estimated height differences would contain systematic errors depending on the slant range position and/or the elevation height. These systematic errors might cause underestimation to some extent. Through the comparison between the measured height differences and truth data, these two possibilities should be discriminated in future studies.

5 Conclusions

The recognition of landslides and making their inventory map are urgent tasks not only to support damage estimation but also for planning rescue and restoration activities (Plank 2014; Plank et al. 2016). To date, various studies utilizing SAR data for landslide detection have been reported. Among the methods utilizing SAR data, those based on height differences accompanying landslides seem attractive since they may successively contribute to damage estimation through a volumetric estimation of landslides. In this context, we propose a landslide detection method utilizing height differences derived from pre- and post-event Pi-SAR2 DEMs combined with amplitude differences. The proposed method is applied to the landslides accompanying the 2016 Kumamoto earthquake, and the accuracy of the detection result is assessed using truth data. Through the application and accuracy assessment, it is demonstrated that the detection ability improves with the utilization of SAR DEMs with a higher altitudinal resolution. In addition, it is demonstrated that the incorporation of amplitude

differences is effective for reducing the number of outliers that appear in the height difference map. The overall accuracy and kappa coefficient for the two scenes including landslides are 87%, 0.60 and 95%, 0.46, respectively. Although the reliability of the proposed method is moderate, as evaluated on the basis of these kappa coefficients, most of the cultivation and residential areas are correctly filtered out, and large- and medium-scale landslides are detected so that the inventory maps derived from the proposed method should be effective at the initial stage of planning rescue and restoration activities. The reasons why the reliability is not good but only moderate are that small-scale landslides cannot be detected and medium-scale ones are imperfectly detected. There are two possible reasons for this. One is that the height differences in these areas are actually not greater than the 5 m threshold. The other is that they are underestimated owing to problems of the estimation method itself. To improve the landslide detection accuracy of the proposed method, these two possibilities should be discriminated in future studies though the comparison between the estimated height changes with truth data.

Compliance with ethical standards

Conflict of interest The authors declare that they have no conflict of interest.

References

Arturi A, Del Frate F, Lategano E et al (2003) The 1998 Sarno (Italy) landslide from SAR interferometry. In: Proceedings of FRINGE 2003 workshop. Frascati, Italy, 1–5 December 2003

Cao YG, Yan LJ, Zheng ZZ (2008) Extraction of information on geology hazard from multi-polarization sar images. Int Arch Photogramm Remote Sens Spat Inf Sci 37:1529–1532

Christophe E, Chia AS, Yin T, Kwoh LK (2010) 2009 Earthquakes in sumatra: The use of L-band interferometry in a SAR-hostile environment. In: Proceedings of the IEEE IGARSS. Honolulu, HI, USA, 25-30 July 2010, pp 1202–1205

Congalton RG (1991) A review of assessing the accuracy of classifications of remotely sensed data. Remote Sens Environ 37:35–46. https://doi.org/10.1016/0034-4257(91)90048-b

Cruden DM (1991) A simple definition of a landslide. Bull Int Ass Eng Geol 43:27–29. https://doi.org/10.1007/bf02590167

Dai FC, Lee CF, Ngai YY (2002) Landslide risk assessment and management: an overview. Eng Geol 64:65–87. https://doi.org/10.1016/s0013-7952(01)00093-x

Dong Y, Li Q, Dou A, Wang X (2011) Extracting damages caused by the 2008 Ms 8.0 Wenchuan earthquake from SAR remote sensing data. J Asian Earth Sci 40:907–914. https://doi.org/10.1016/j.jseaes.2010.07.009

Furuta R, Sawada K (2013) Case study of landslides recognition using dual/quad polarization data of ALOS/PALSAR. In: Proceedings of APSAR. Tsukuba, Japan, 23-27 September 2013, pp 481–484

Ghiglia DC, Pritt MD (1998) Two-dimensional phase unwrapping: theory, algorithms, and software. Wiley, New York

Kawamura M, Tsujino K, Tsujiko Y, Tanjung J (2011) Detection method of slope failures due to the 2009 sumatra earthquake by using TerraSAR-X images. In: Proceedings of the IEEE IGARSS. Vancouver, BC, Canada, 24–29 July 2011, pp 4292–4295

Kobayashi T, Umehara T, Uemoto J et al (2012) Performance evaluation on cross-track interferometric SAR function of the airborne SAR system (PI-SAR2) of NICT. In: International Geoscience and Remote Sensing Symposium (IGARSS)

Kobayashi T, Kojima S, Umehara T et al (2016) Pleliminary results of repeat pass interferometry of the X-band airborne SAR system (pi-sar2) of NICT. In: Proceedings of the IEEE IGARSS. Beijing, China, 10–15 July 2016

Kojima S, Umehara T, Kobayashi T et al (2014) Preliminary analysis of cross-track interferometry by synthetic beam of two antennas of along-track interferometric SAR. In: Proceedings of the IEEE IGARSS. Quebec City, QC, Canada, 1–18 July 2014, pp 366–369

Liao JJ, Shen GZ (2009) Detection of land surface change due to the Wenchuan earthquake using multi-temporal advanced land observation satellite-phased array type L-band synthetic aperture radar data. J Appl Remote Sens. https://doi.org/10.1117/1.3142466

Liu W, Yamazaki F (2015) Detection of landslides due to the 2013 Thypoon Wipha from high-resolution airborne SAR images. In: Proceedings of the IEEE IGARSS. Milan, Italy. 26-31 July 2015, pp 4244–4247

Lu Z, Dzurisin D, Jung H-S et al (2010) Radar image and data fusion for natural hazards characterisation. Int J Image Data Fusion 1:217–242. https://doi.org/10.1080/19479832.2010.499219

Massonnet D, Feigl KL (1998) Radar interferometry and its application to changes in the Earth's surface. Rev Geophys 36:441–500. https://doi.org/10.1029/97rg03139

Metternicht G, Hurni L, Gogu R (2005) Remote sensing of landslides: an analysis of the potential contribution to geo-spatial systems for hazard assessment in mountainous environments. Remote Sens Environ 98:284–303. https://doi.org/10.1016/j.rse.2005.08.004

Nadai A, Uratsuka S, Umehara T et al (2009) Development of X-band airborne polarimetric and interferometric SAR with sub-meter spatial resolution. In: Proceedings of the IEEE IGARSS. Cape Town, South Africa, 12–17 July 2009, pp II-913–II-916

Oliver C, Shaun Q (2004) Understanding Synthetic Aperture Radar Images. SciTech Publishing, Raleigh

Plank S (2014) Rapid damage assessment by means of multi-temporal SAR-A comprehensive review and outlook to sentinel-1. Remote Sens 6:4870–4906. https://doi.org/10.3390/rs6064870

Plank S, Twele A, Martinis S (2016) Landslide mapping in vegetated areas using change detection based on optical and polarimetric SAR data. Remote Sens 8:307. https://doi.org/10.3390/rs8040307

Richards MA (2007) A beginner's guide to interferometric SAR concepts and signal processing. IEEE Aerosp Electron Syst Mag 22:5–29. https://doi.org/10.1109/maes.2007.4350281

Scaioni M, Longoni L, Melillo V, Papini M (2014) Remote sensing for landslide investigations: an overview of recent achievements and perspectives. Remote Sens 6:9600–9652. https://doi.org/10.3390/rs6109600

Shibayama T, Yamaguchi Y, Yamada H (2015) Polarimetric scattering properties of landslides in forested areas and the dependence on the local incidence angle. Remote Sens 7:15424–15442. https://doi.org/10.3390/rs71115424

Tang Y, Zhang Z, Wang C et al (2015) Characterization of the giant landslide at Wenjiagou by the insar technique using TSX-TDX CoSSC data. Landslides 12:1015–1021. https://doi.org/10.1007/s10346-015-0616-z

Tobita M, Fujiwara S, Murakami M et al (1999) Accurate offset estimation between two SLC images for SAR interferometry. J Geod Soc Jpn 45:297–314

Yagi Y, Okuwaki R, Enescu B (2016) Rupture process of the 2016 Kumamoto earthquake in relation to the thermal structure around Aso volcano. Earth Planets Sp. https://doi.org/10.1186/s40623-016-0492-3

Zhao C, Zhang Q, Yin Y et al (2013) Pre- co- and post- rockslide analysis with ALOS/PALSAR imagery: a case study of the Jiweishan rockslide, China. Nat Hazards Earth Syst Sci 13:2851–2861. https://doi.org/10.5194/nhess-13-2851-2013